Article

A Core and Valence-Level Spectroscopy Study of the Enhanced Reduction of CeO_2 by Iron Substitution—Implications for the Thermal Water-Splitting Reaction

Hicham Idriss

Karlsruhe Institute of Technology (KIT), 76344 Eggenstein-Leopoldshafen, Germany; hicham.idriss@kit.edu

Abstract: The reduction of Ce cations in CeO_2 can be enhanced by their partial substitution with Fe cations. The enhanced reduction of Ce cations results in a considerable increase in the reaction rates for the thermal water-splitting reaction when compared to CeO_2 alone. This mixed oxide has a smaller crystallite size when compared to CeO_2, in addition to a smaller lattice size. In this work, two Fe-substituted Ce oxides are studied ($Ce_{0.95}Fe_{0.05}O_{2-\delta}$ and $Ce_{0.75}Fe_{0.25}O_{2-\delta}$; $\delta < 0.5$) by core and valence level spectroscopy in their as-prepared and Ar-ion-sputtered states. Ar ion sputtering substantially increases Ce4f lines at about 1.5 eV below the Fermi level. In addition, it is found that the XPS Ce5p/O2s ratio is sensitive to the degree of reduction, most likely due to a higher charge transfer from the oxygen to Ce ions upon reduction. Quantitatively, it is also found that XPS Ce3d of the fraction of Ce^{3+} (u_o, u' and v_o, v') formed upon Ar ion sputtering and the ratio of Ce5p/O2s lines are higher for reduced $Ce_{0.95}Fe_{0.05}O_{2-\delta}$ than for reduced $Ce_{0.75}Fe_{0.25}O_{2-\delta}$. XPS Fe2p showed, however, no preferential increase for Fe^{3+} reduction to Fe^0 with increasing time for both oxides. Since water splitting was higher on $Ce_{0.95}Fe_{0.05}O_{2-\delta}$ when compared to $Ce_{0.75}Fe_{0.25}O_{2-\delta}$, it is inferred that the reaction centers for the thermal water splitting to hydrogen are the reduced Ce cations and not the reduced Fe cations. These reduced Ce cations can be tracked by their XPS Ce5p/O2s ratio in addition to the common XPS Ce3d lines.

Keywords: cerium oxide reduction; cerium cation substitution; x-ray valence band spectroscopy; thermogravimetric analysis; XPS Ce4f; XPS Fe2p

1. Introduction

Cerium oxide is one of the most known stable redox oxides. This property makes it the oxide support of choice for automobile catalytic converters (three-way catalyst, TWC), which have been in use for decades [1]. The relative ease with which it goes through reduction and re-oxidation cycles while maintaining its crystallographic structure (fluorite) is the main reason for this [2]. This particular property also makes it among the best-known support oxides for other redox catalytic reactions, such as the water–gas shift reaction (WGSR) [3]. For both reactions (WGSR and TWC), the reduction of CeO_2 occurs chemically. In other words, the input of energy is from a hydrocarbon in the case of the TWC and from CO in the case of the WGSR [4]. This allows the redox cycle to occur at relatively low temperatures relevant for catalytic reactions.

CeO_2 is also one of the most active and stable known oxides for thermochemical water splitting to H_2 and O_2 for energy applications [5]. For this reaction, however, the reduction is considered in the absence of a reducing agent and where heat (from the sun) is the sole energy input. Temperatures typically above 1500 °C are needed for an appreciable reduction to take place [6]. This adds a considerable strain to the process, and so far, its possible applications would be very costly and largely unpractical. To this end, much work addressing the reduction of CeO_2 in order to understand its steps at the fundamental and applied levels has been pursued.

One of the strategies to enhance the reduction of CeO_2 is to mix it with other oxides. This may be grouped into three categories.

1. Size substitution (iso-valency): Compensation for lattice expansion. Upon the reduction of Ce^{4+} cations to Ce^{3+}, the unit cell of CeO_2 increases. This is because the eight-coordinated Ce^{4+} cation size is about 1 Å, while the eight-coordinated Ce^{3+} cation size is about 1.1 Å. Substituting some of the Ce^{4+} cations with metal cations with the same formal oxidation state (M^{4+}) but a smaller size compensates partly for the lattice expansion. This is particularly successful when Zr^{4+} cations are used (size ca. 0.8 Å) [7,8]. While the substitution is valid up to about 50% (maintaining the fluorite structure of CeO_2) [9], phase segregation occurs at high temperatures (at 1000 °C or so) [10].

2. Charge transfer: substitution with oxidizable higher-valence cations. In this case, a fraction of Ce^{4+} cations is substituted with metal cations that can donate electrons and themselves be oxidized [11]. The substitution of Ce^{4+} with U^{4+} was found to enhance the reduction of CeO_2, particularly at low levels [12,13]. Upon the removal of an oxygen atom, three Ce^{3+} cations are formed (instead of two), and one U^{4+} cation is oxidized to a U^{5+} action. In addition, the fact that both oxides, CeO_2 and UO_2, have a fluorite structure and both cations have the same size makes them miscible for the entire ratio range [14]. The optimal dosing for the reduction of Ce cations is not clear yet, and neither is the temperature at which phase segregation occurs.

3. Charge compensation (alio-valencies): lattice distortion. While the substitution of Ce^{4+} with metal cations of a lower oxidation state will create vacancies, these vacancies are not charged. In other words, there is no increase in electron charge. The effect is, however, clear; for example, the substitution of Ce^{4+} cations with Fe^{3+} cations (up to about 20%) results in a considerable reduction of the host oxide [15]. This is thought to be due to the distortion of the lattice structure, making it less stable and therefore enabling further reduction [16]. In recent work, this was found to be the case for high-temperature reduction (with no chemical input). Yet, considerable phase segregation occurred after one TCWS reaction cycle [17].

In the case of alio-valence substitution (the word substitution is sometimes mentioned as doping; strictly speaking, doping is the addition of another element in ppm or ppb amounts to change its electronic properties and is not necessary added as a substitution), a large number of elements were studied, and most showed that Ce^{4+} reduction to Ce^{3+} was enhanced. These include Co (4%) co-precipitation for the photoreduction of CO_2 to CH_4 [18], Co (23%) for COS hydrolysis [19], Co (20%) for Hg removal [20], Pr (10–50%), in which Pr^{3+} increases the creation of oxygen vacancies and Pr^{4+} increases the oxygen storage capacity [21] and Mn (12%), enhancing oxygen mobility via vacancy formation [22]. Computationally, a large body of work was also conducted to study the creation of oxygen vacancies upon alio-valent cation substitution. These include the following: Mn (DFT + U and HSE06) [23], Cu (DFT + U) [24], Ni (DFT + U and HSE06) [25] and (DFT + U) [26], and other rare earth elements (Sc, Y, Gd, La) by DFT + U and Monte Carlo simulations [27].

Focusing on Fe substitution, considerable work at the experimental and theoretical levels has been conducted, and a few studies are mentioned here. Fe substitution of less than 30% increased the number of oxygen vacancies [28] and the selective catalytic reduction of NO to NH_3. The DFT +U results of Fe-doped CeO_2 (111) indicated that the oxygen vacancy formation energy is lower when compared to ceria alone and that Fe tends to be the center of the oxygen vacancy clusters [29]. Improved CO conversion over a CeO_2-Fe_2O_3 mixed oxide was also seen and attributed to the formation of more mobile oxygen atoms in the redox cycle [30]. Fe substitution was previously studied for the thermochemical water-splitting reaction among other cation substitutions (Mn, Ni, and Cu), and the CeO_2 substitute was found to be still active after four reaction cycles (O_2 and H_2 release) [31] at 1273 K (1000 °C). In another work for the same reaction, Fe at 5% was tested at 1550 °C and was found to be more active (a higher production rate per unit weight) and faster (a higher rate of release of hydrogen) than CeO_2 alone. However, considerable phase segregation

occurred due to the very high thermal reduction, 1550 °C, after one cycle of reaction [17]. This work is an extension of a previous one, focusing on the changes that occurred upon the reduction of Ce cations in the presence of Fe cations. Since during the reduction of Ce^{4+} cations to Ce^{3+} cations, Fe^{3+} cations would also be reduced to Fe^{2+} and Fe^0, monitoring the changes that occur for both elements is needed. Also, as it will be shown, it seems that the ratio of the XPS Ce5p/O2s shallow core level lines is sensitive to the degree of reduction.

2. Results and Discussion

The prepared CeO_2 and Fe-substituted CeO_2 were studied in some detail previously by TEM, EELS, XRD and TPR, among other methods [17]. Figure 1 gives a brief description of $Ce_{0.95}Fe_{0.05}O_{2-\delta}$ and $Ce_{0.75}Fe_{0.25}O_{2-\delta}$. Both oxides are composed of small crystallites upon calcination (500 °C). These were about 8 and 5 nm in size for $Ce_{0.95}Fe_{0.05}O_{2-\delta}$ and $Ce_{0.75}Fe_{0.25}O_{2-\delta}$, respectively. The TEM images show that they are dominantly (111) terminated. These crystals are identical to those of CeO_2 [17], which is composed of crystallites of about 14 nm in size. The decrease in crystallite sizes upon Fe substitution is also similar to that previously reported by others [32]. This is most likely due to the change in ionicity of the sol–gel medium during the precipitation [33]. Also, as seen, the only observed phase (XRD, TEM) is the fluorite one. The unit cells show a slight decrease due to Fe substitution (0.543, 0.539 and 0.536 nm for CeO_2, $Ce_{0.95}Fe_{0.05}O_{2-\delta}$ and $Ce_{0.75}Fe_{0.25}O_{2-\delta}$, respectively). As shown in Figure 1C,D, up to 700 °C, there is a gradual, small increase in the lattice and crystallite sizes. An abrupt change occurs at 900 °C, where considerable sintering is seen and is accompanied by the appearance of lines due to Fe oxides, indicating the beginning of the phase segregation process, which was accentuated by 1100 °C.
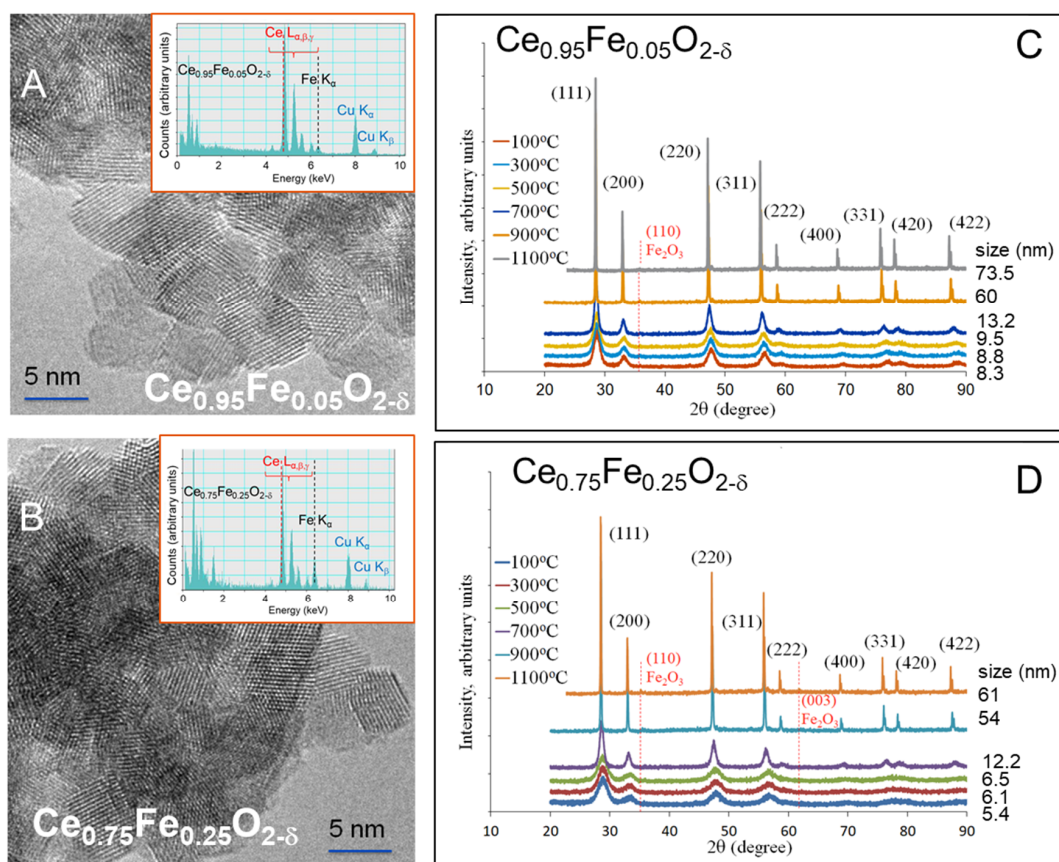
Figure 1. Transmission electron microscopy (TEM) (A and B), energy-dispersive x-ray (EDX) (insets in (**A,B**) and x-ray diffraction (XRD) of (**C**) $Ce_{0.95}Fe_{0.05}O_{2-\delta}$ and (**D**) $Ce_{0.75}Fe_{0.25}O_{2-\delta}$. The figures are adapted with permission from [17].

Figure 2A,B present the valence band and shallow core levels (Ce5p, O2s, and Ce5s) of $Ce_{0.75}Fe_{0.25}O_{2-\delta}$ and $Ce_{0.95}Fe_{0.05}O_{2-\delta}$ before and after 1, 2 and 5 min of argon ion sputtering. The reduction of the oxides was conducted by Ar ion sputtering. This method has advantages and disadvantages when compared to hydrogen reduction or thermal reduction. Thermal reduction of these oxides requires heating to at least 1500 °C. The mixed oxide at this temperature largely segregates, and therefore, the analysis would not be useful. Reduction using molecular hydrogen in UHV is not possible because of its very low sticking coefficient on oxides. It is possible to reduce oxides with atomic hydrogen, but this method was not available. Argon ion sputtering to reduce oxides relies on the mass difference between the metal cation and oxygen anions and the stability of the reduced phase thus created at given experimental conditions. Ce^{3+}, Fe^{2+}, and Fe^0 are stable in UHV conditions. In other words, once formed, not much change is seen within the investigation time (a few hours). The drawback of Ar ion sputtering is the loss of surface structure (the formation of an amorphous layer due to the high energy ion bombardment used, in this work, 1 kV).
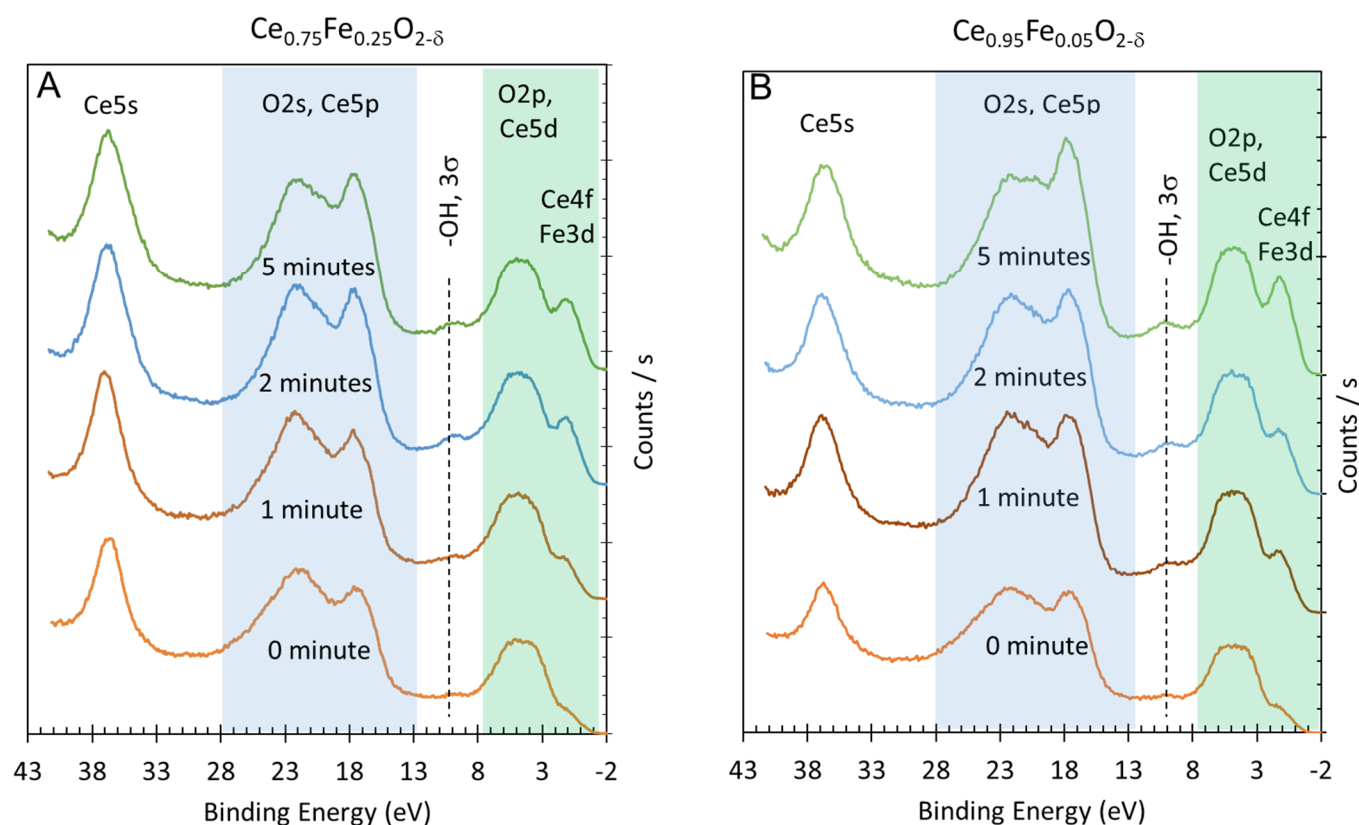

Figure 2. (**A**) Valence band XPS (green shaded) and Ce5p, O2s (blue-shaded) and Ce5s spectra of $Ce_{0.75}Fe_{0.25}O_{2-\delta}$ before (0 min) and after argon ion sputtering (x min). (**B**) Valence band XPS (green shaded) and Ce5p, O2s (blue-shaded) and Ce5s spectra of $Ce_{0.95}Fe_{0.05}O_{2-\delta}$ before (0 min) and after argon ion sputtering (x min).

The initial spectra of the as-prepared oxides (0 min) are dominated by the O2p, O2s, Ce5p and Ce5s lines and are hardly distinguishable for both oxides. There are traces of unavoidable surface hydroxyls (-OH, 3 σ) at a binding energy of ca. 10 eV and some contribution from reduced Ce cations (Ce4f, Ce^{3+}) and reduced Fe cations (Fe3d, oxidation state < +3), both below the O2p band with a binding energy of 0.5–2 eV. Upon argon ion sputtering, three changes are noticeable: (i) An increase in the signal before the O2p reductions (due to increased concentrations of Ce^{3+} and Fe^{+x}, x < +3). (ii) An increase in surface hydroxyls. (iii) A relative increase in Ce5p signal with respect to the O2s signal. For

(i), the increase is expected and is treated in more detail in this work to extract quantitative information. For (ii), the increase has been seen before and is linked to the increase in the sticking coefficient of dissociatively adsorbed water (in the background) over a reduced metal oxide when compared to its stoichiometric form. The ion bombardment causes a reduction due to oxygen removal (as atoms), and the remaining electrons (two for each oxygen atom removed) are transferred to Ce^{4+} (and Fe^{3+}) to reduce them. The creation of the oxygen vacancy leads to the preferential dissociative adsorption of a water molecule. This results in the formation of two pairs of surface hydroxyls for each oxygen vacancy healed. This is not the purpose of this study and will not be further treated. For (iii), this observation is unexpected and is treated here qualitatively.

Figure 3A,B present the valence band region, in which the signal below the O2p orbital was fitted by two peaks: the first at about 0.4 eV and the second at ca. 1.5 eV below the Fermi level. There are no noticeable changes in the large O2p lines' shapes with sputtering time. For both oxides, the signal attributed to the Ce4f orbital is higher than that of the Fe3d orbital. The increase of the XPS Ce4f signal upon reduction is more pronounced in the case of a low Fe concentration when compared to the other oxides. This is consistent with the other core levels (see below) as well as with the TCWS results (also see below). Computing the peak areas of the two peaks seems to indicate that there is no incentive to further reduce Ce cations with a higher % of Fe. At a low Fe %, increasing the reduction time affects mostly the Ce cations, while at a higher Fe %, it favors Fe reduction. This might be simply due to the probability of hitting the atoms during bombardment. At a high Fe %, the probability of oxygen removal adjacent to Fe atoms is high, and therefore more Fe is reduced, while at a low Fe %, the oxide is more homogeneous and the chemical effect on the reduction is higher.
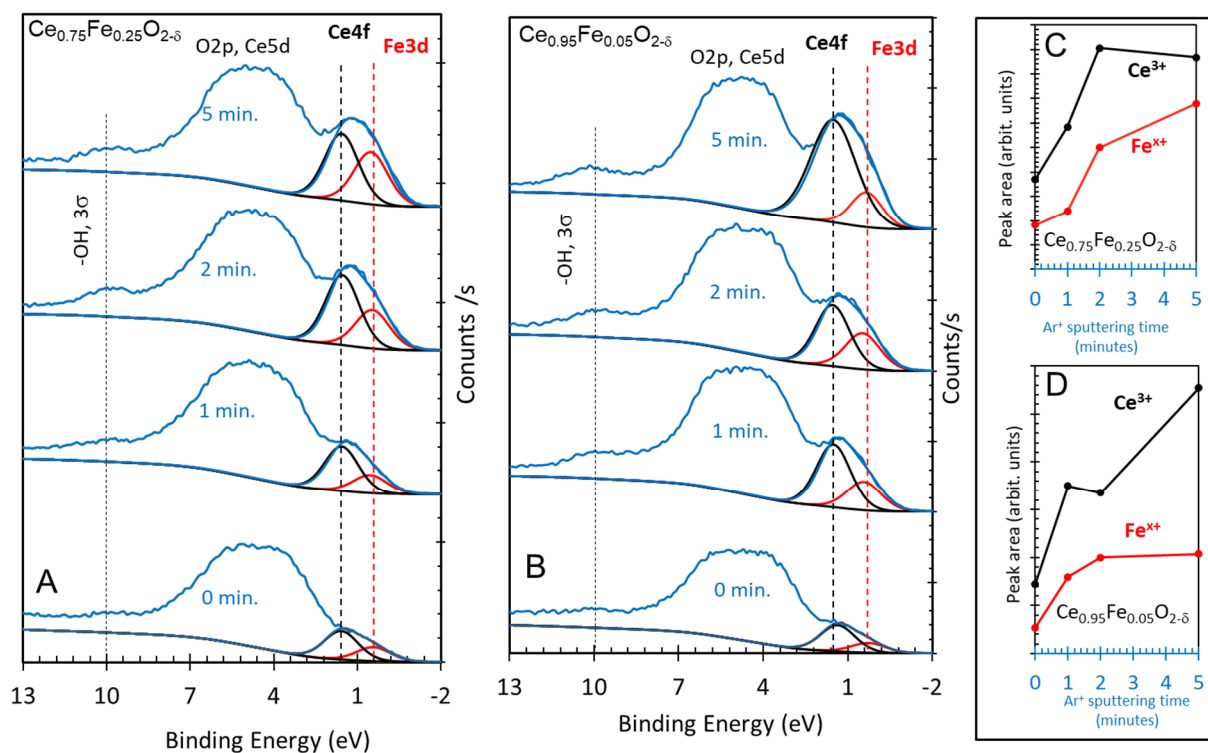
Figure 3. (**A**) Valence band XPS of as-prepared $Ce_{0.75}Fe_{0.25}O_{2-\delta}$ after 1, 2 and 5 min of Ar ion sputtering. (**B**) Valence band XPS of as-prepared $Ce_{0.95}Fe_{0.05}O_{2-\delta}$ after 1, 2 and 5 min of Ar ion sputtering. (**C,D**) Computed peak areas of fitted Ce4f (FWHM = 1.5 eV) and Fe3d (FWHM = 1.5 eV) signals.

Figure 4A,B present the valence band together with the Ce5p and O2s lines. The spectra are baseline-subtracted and then normalized to highlight the differences. The ion sputtering of both oxides results in a preferential increase in the Ce5p signal when compared to the

O2s lines. In addition, the O2s line becomes narrower upon ion sputtering. There is no noticeable shift in the binding energy before or after ion bombardment. Similar experiments were conducted on CeO_2, and no change was seen (SI Figure S1). Obtaining quantitative information from polycrystalline oxides is more difficult because of the unavoidable grain boundary effect (channeling) and shadowing, both of which would make ion sputtering less efficient when compared to sputtering thin films or single crystals. Nevertheless, some qualitative information may be drawn from comparisons to previous work conducted by others. One of the most relevant to this present work is a study on the ion bombardment [34] of CeO_2, in which it was shown (Figure 3a,b of ref. [34]) that the relative ratio is indeed increased in favor of the Ce5p orbital. The exact position of the O2s orbital with respect to the $Ce5p_{1/2}$ orbital is not clear. In this work, it is put after the $Ce5p_{1/2}$ lines in line with other work, although others have put it in between the $Ce5p_{3/2}$ and $Ce5p_{1/2}$ energy positions based on the relativistic computation of CeO_8 and $Ce_{63}O_{216}$ clusters [35]. One of the motivations of studies of the O2s and Ce5p lines is charge transfer, where these lines, because of their quasi-degenerate energy positions, are sensitive to the oxidation state of Ce cations. The spectra in Figure 4 are similar to those reported for a thin film of CeO_2 grown on Rh(111) [36] excited with photon energy equal to 125 eV (Ce4d-Ce4f resonance). The spectra are also similar to those of irradiated (with Xe ions) CeO_2 thin film and bulk [34]. The authors pointed out the final state effect ($3d^9 4f^1 OVMO^{-1}$ (outer valence molecular orbital, OVMO) and $3d^9 5p^5 np^1$ (inner valence molecular orbital, INVO)). In another work [33], the authors indicated the Ce5p atomic orbitals participate in the formation of both OVMO and IVMO, where a large part of the latter is taken by the filled $Ce5p_{1/2}$, $5p_{3/2}$ and O2s atomic shells.
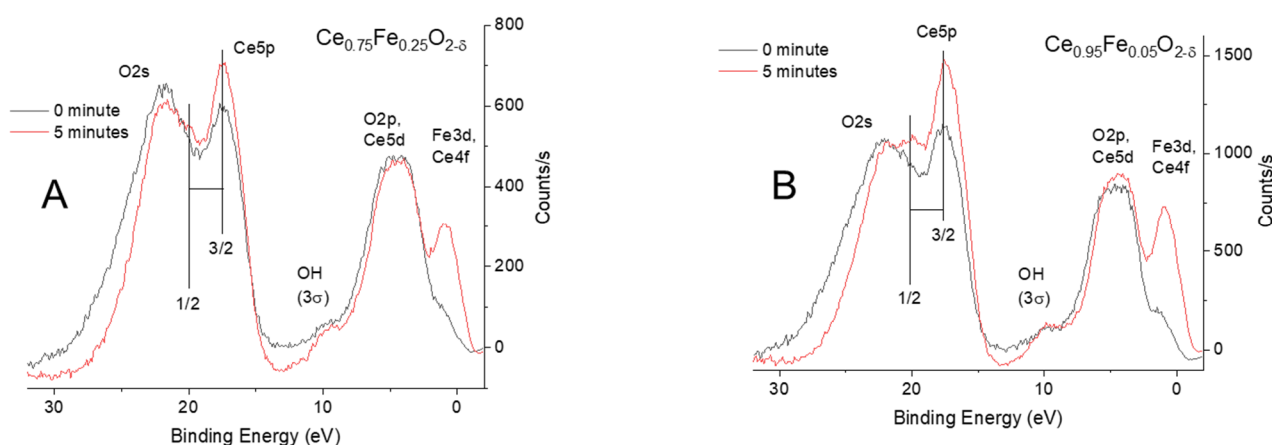

Figure 4. (**A**) Normalized valence band XPS and the Ce5p and O2s spectra of $Ce_{0.75}Fe_{0.25}O_{2-\delta}$ before (0 min) and after 5 min of argon ion sputtering. (**B**) Normalized valence band XPS and the Ce5p and O2s spectra of $Ce_{0.95}Fe_{0.05}O_{2-\delta}$ before (0 min) and after 5 min of argon ion sputtering. Note the change in intensity of the Ce5p signal when compared to the O2s signal.

The spectra in Figure 4 are fitted in Figure S2. Four peaks are considered ($Ce5p_{3/2,1/2}$ and two for O2s). The two O2s peaks are for the two different (bulk and surface oxygen atoms) environments and are separated by about 2.5 eV (similar to the O1s signal). It is to be noted that similar attribution was given for the O2s signal to clean and glycine-dosed surfaces, where the high-binding O2s line is due to surface hydroxyls and carboxylates [37].

Figure 5 presents the XPS Ce3d spectra of the Ce cations in the fresh and Ar-ion-reduced samples. The presence of both oxidation states of Ce cations is clear even in the freshly prepared oxides. However, in this case, the Ce^{3+} cation concentration is small, and they most likely reside in deeper layers below the surface. In Figure 5 the lines' positions and attributions are shown ($3d_{5/2}$: u, u″ and u‴, and $3d_{3/2}$: v, v″ and v‴ for Ce^{4+} cations, and $3d_{5/2}$: u_o and u′ and $3d_{3/2}$: v_o and v′ for Ce^{3+} cations). Upon fitting these peaks, information can be obtained. In Figure 5 and the inset table, a comparison between the

fresh and the most reduced samples is made. The presence of Fe at a 5% concentration resulted in a more pronounced Ce^{3+} concentration when compared to the presence of Fe at a 25% concentration. This is in line with the valence band results presented in Figures 2 and 3. CeO_2 alone showed a very mild increase upon reduction; this is also in line with the virtually no change in the Ce5p/O2s lines in Figure 1. Ar ion sputtering relies on the momentum transfer of incoming ions (in this case, 1 keV of kinetic energy), which results in breaking the chemical bonds. As such, there should be no difference between CeO_2 and Fe-substituted CeO_2 since the incoming ions have much more energy than the chemical bond, assuming complete energy transfer. However, this is a cascade reaction where the energy transfer occurs consecutively, and therefore the last steps of an incoming ion (before it leaves the material or is implanted in it irreversibly) would be more efficient for weaker bonding. This is particularly important for polycrystalline nanoparticles, where interparticle pore diffusion dominates.
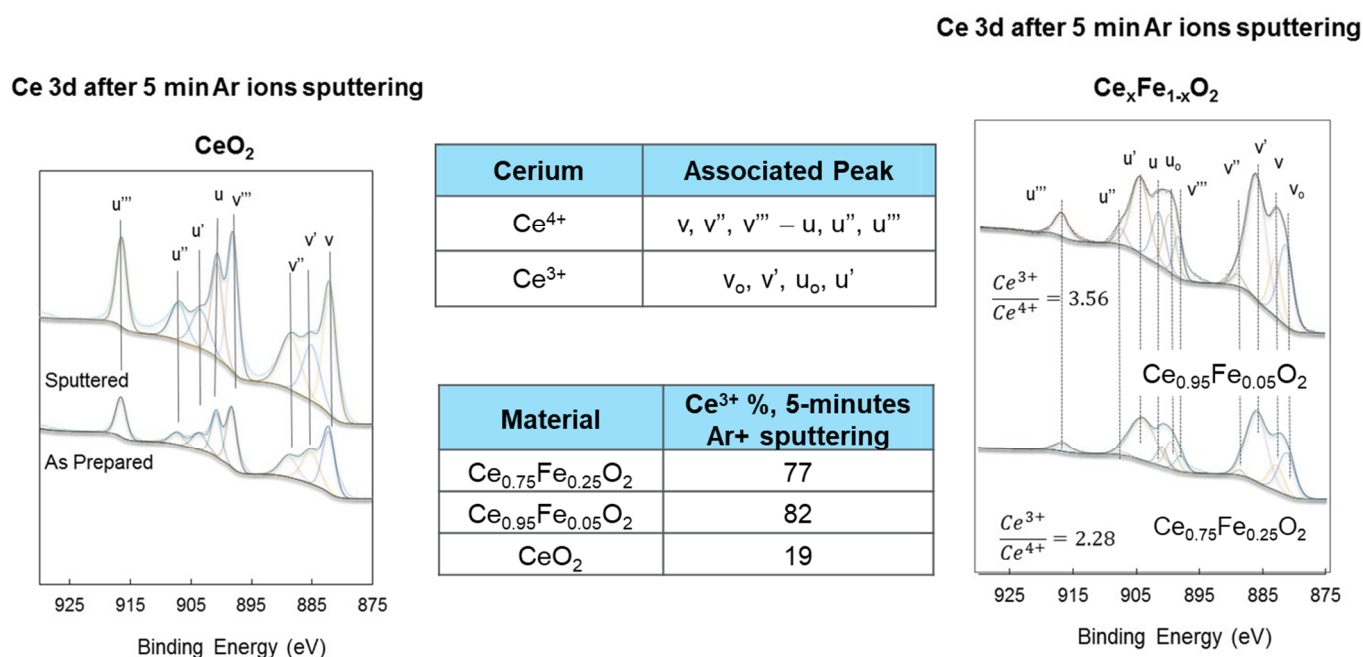
Figure 5. XPS Ce3d spectra of as-prepared CeO_2 (left panel), $Ce_{0.75}Fe_{0.25}O_{2-\delta}$ and $Ce_{0.95}Fe_{0.05}O_{2-\delta}$ (right panel) after 5 min of Ar ion sputtering. Also shown are the computed contributions of the Ce^{3+} and Ce^{4+} cations.

Based on the Ce4f/O2p, Ce5p/O2s and Ce3d (for Ce^{4+} and Ce^{3+}) XPS signals, Table 1 is constructed to provide an estimate of the reduction of Ce cations in this work.

Table 1. Extracted quantitative values from XPS Ce3d, Ce4f, Ce5p and Fe2p spectra and thermochemical water splitting to hydrogen over reduced oxides. The XPS data are those for reduced oxides after 5 min of argon ion sputtering. The hydrogen production data are at 700 °C under N_2 from prior hydrogen-reduced oxides at 700 °C.

Oxide	Ce^{3+}/Ce^{4+} (Ce3d)	$[Ce4f + Fe3d^x]/O2p$	Fe^0/Fe^{3+} (Fe2p)	Ce5p/O2s	H_2 Production (mol/g)
CeO_2	0.2	-	-	0	0.2×10^{-6}
$Ce_{0.75}Fe_{0.25}O_{2-\delta}$	2.3	0.3	0.5	1.6	7.4×10^{-6}
$Ce_{0.95}Fe_{0.05}O_{2-\delta}$	3.6	0.4	0.6	1.75	11.4×10^{-6}

The XPS core levels of iron oxides are among the most studied for oxides [38]. There are three common oxidation states for the oxides: Fe^{3+}, such as in Fe_2O_3, Fe^{2+}, such as in

FeO, and Fe_3O_4, in addition to metallic Fe. The spectra are complicated by the presence of satellites [39–41], iron hydroxide (FeOOH) [42,43] and many multiplets [44]. The binding energy of the XPS Fe2p signal is about 707 eV for metallic iron, 710 eV for Fe^{2+} and 711 eV for Fe^{3+} cations. In the present study, a further complication arises from the presence of Ce Auger lines in the Fe2p region. Moreover, although charge neutralization was used, the as-prepared oxide always had wider peaks when compared to that reduced upon ion sputtering. Therefore, peak areas are to be taken with an estimate of 20% errors and binding energies within a 0.5 eV accuracy. Both oxides show very similar spectra and trends upon reduction. While, as expected, the as-prepared oxides contained Fe^{3+} cations, they, however, also contained Fe^{2+} and some metallic iron. Some small % of Fe^{2+} might be formed during the preparation (Figure 6). The presence of metallic iron was not expected and is most likely due to interstitial atoms formed due to strong lattice distortion. The insets in both figures show the trend during the reduction. It was opted chose to subtract the Fe^{2+} and Fe^0 contributions of the as-prepared oxides to see the trend. In both cases, the amount of Fe^{2+} increases, similar to a previous study [45], then decreases to zero, indicating that within the reduction time studied, all reducible Fe^{3+} cations were transformed to metallic Fe. In line with the valence band results, it appears that both Ce^{4+} and Fe^{3+} cations are more efficiently reduced when in small amounts ($Fe_{0.05}$), as seen in Figure 6B, although the difference is not dramatic.
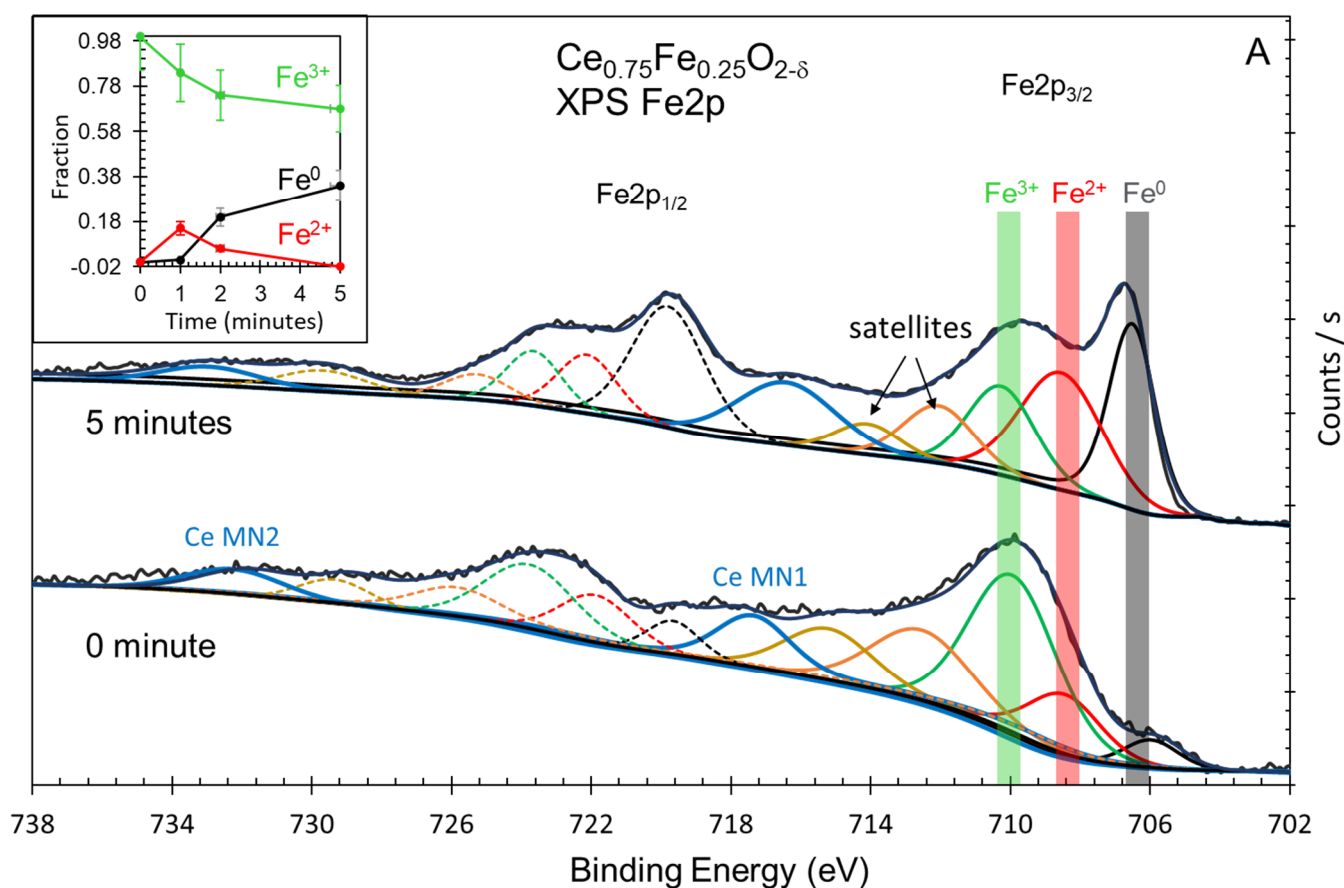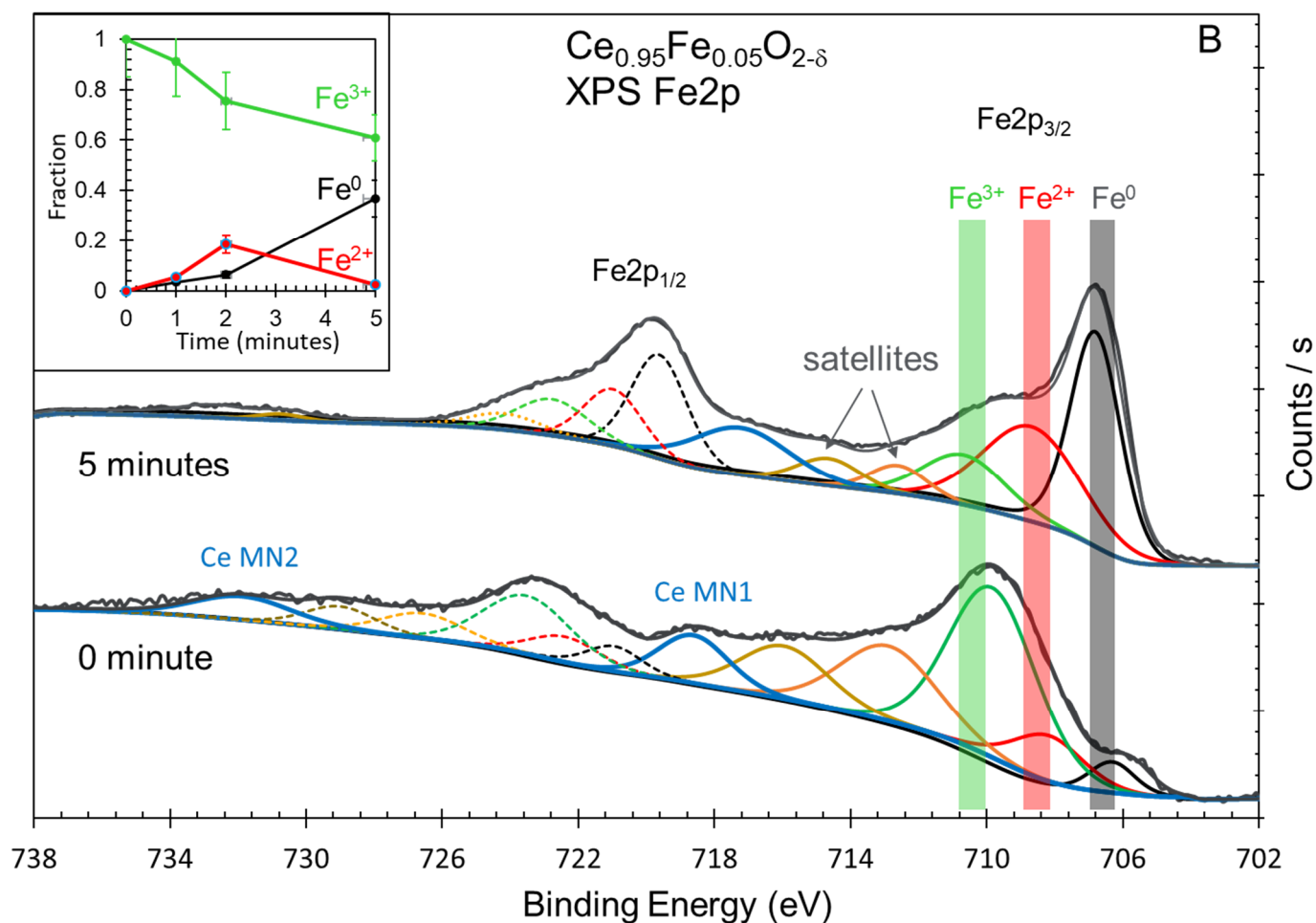

Figure 6. *Cont.*

Figure 6. (**A**) XPS Fe2p spectra of as-prepared $Ce_{0.75}Fe_{0.25}O_{2-\delta}$ after 5 min of Ar ion sputtering. (**B**) XPS Fe2p spectra of as-prepared $Ce_{0.95}Fe_{0.05}O_{2-\delta}$ after 5 min of Ar ion sputtering. Insets in (**A**,**B**): quantitative analysis of XPS Fe2p spectra of $Ce_{0.75}Fe_{0.25}O_{2-\delta}$ and $Ce_{0.95}Fe_{0.05}O_{2-\delta}$ before and after sputtering at the indicated time.

Figure 7 presents the hydrogen production of the three oxides from water at 700 °C. The point of the figure is to relate the production to the observed reduced states of the oxides. Because, as indicated, the two mixed oxides are not segregated when heated to this temperature, a link to the spectroscopic measurements would be relevant even though, as such, it is not practical (since the oxides were previously reduced with molecular hydrogen). CeO_2 alone shows negligible activity, while the Fe-substituted cerium oxides are active (the production is given in Table 1). The activity of the $Ce_{0.95}Fe_{0.05}O_{2-\delta}$ catalyst is almost twice that of the $Ce_{0.75}Fe_{0.25}O_{2-\delta}$ catalyst. This suggests that the activity is more linked to Ce^{3+} than to Fe^0 (based on the XPS Ce3d and XPS Ce5p/O2s spectra). This is because the content of Fe^0 in both reduced oxides was similar (XPS Fe2p), while that of Ce^{3+} was higher for $Ce_{0.95}Fe_{0.05}O_{2-\delta}$ than for $Ce_{0.75}Fe_{0.25}O_{2-\delta}$.
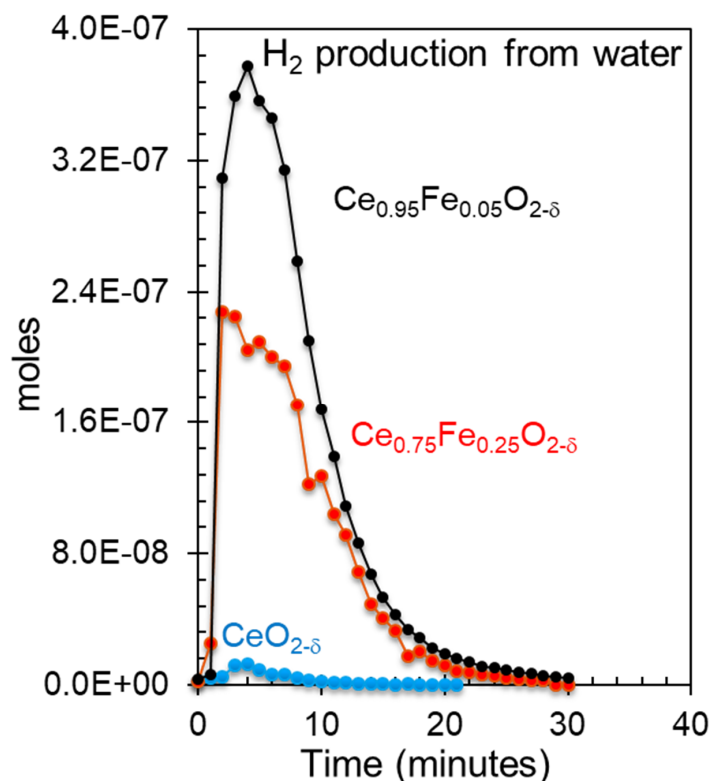
Figure 7. Hydrogen production from water over CeO_2, $Ce_{0.75}Fe_{0.25}O_{2-\delta}$ and $Ce_{0.95}Fe_{0.05}O_{2-\delta}$, which were previously reduced with hydrogen at 700 °C at one atmosphere.

3. Experimental Section

The CeO_2, $Ce_{0.95}Fe_{0.05}O_{2-\delta}$ and $Ce_{0.75}Fe_{0.25}O_{2-\delta}$ catalysts were synthesized by the co-precipitation method already presented in other work [17]. In brief, cerium (III) nitrate hexahydrate (from Sigma Aldrich, St. Louis, MO, USA) was dissolved in deionized water alone or together with the needed amount of iron (III) nitrate (from Sigma Aldrich). NH_4OH, used as a precipitating agent (70 vol. %), was added to the solution containing the metal cations while stirring until a pH > 9 was reached. After the filtration of the precipitate, it was washed using deionized water until a neutral pH was obtained. The precipitate (in the form of metal hydroxides) was then dried in an oven at 100 °C overnight, then crushed, loaded into a crucible and calcined in air at 500 °C for 12 h with a temperature ramp of 15 °C min^{-1}.

X-ray diffraction (XRD) data were collected using a PANalytical EMPYREAN diffractometer (Malvern, UK) in Bragg–Brentano geometry with Cu K_α excitation at 45 kV and 40 mA and a linear position-sensitive detector. The diffractometer was configured with a 0.25° diverging slit, a 0.5° anti-scattering slit, 2.3° Soller slits, and a Ni filter. Data were acquired in continuous scanning mode over the 2θ range 10–90° at a step interval of 0.01° and 0.5 s per step.

Transmission electron microscopy (TEM) studies were conducted using a Titan ST microscope (FEI company, Hillsboro, OR, USA). It operated at an accelerating voltage of 300 kV and was equipped with a field emission electron gun, a 4k×4k CCD camera, a Gatan imaging filter (GIF), and a Gatan microscopy suite (GMS).

X-ray photoelectron spectroscopy (XPS) was conducted using a Thermo scientific ESCALAB 250 Xi. Spectra (Waltham, MA, USA) were calibrated with respect to the C1s line at 284.7 eV. The Fe2p, O1s, Ce3d, Ce4d, C1s, O2s, Ce5s, Ce5p, and the valence band (O2p, Ce4f and Fe3d) binding energy regions were scanned. The typical acquisition conditions were as follows: pass energy = 20 eV and scan rate = 0.1 eV per 200 ms. Ar^+- bombardment was conducted with an EX06 ion gun at a 1 kV beam energy and a 10 mA emission current.

The sputtered area of 900×900 µm^2 was larger than the analyzed area of 600×600 µm^2. Self-supported oxide disks, approximately 0.5 cm in diameter, were loaded into the chamber. Data acquisition was carried out using the Avantage Data System V5 software. Charge neutralization was used for all the samples (1 eV).

The water-splitting experiments were conducted as follows: 0.25 g of the metal oxide (CeO_2, $Ce_{0.95}Fe_{0.05}O_{2-\delta}$ or $Ce_{0.75}Fe_{0.25}O_{2-\delta}$) was put in a tubular quartz reactor (1/4″ O.D.), then heated to 700 °C for three hours under a hydrogen flow of 20 mL/min at one atmosphere. Then, at 700 °C, the hydrogen flow was stopped and replaced by N_2 at a flow of 30 mL/min. This continued for a period (typically 60 min) until no hydrogen was detected from the line using an online Gas Chromatograph (GC). The GC was equipped with a Thermal Conductivity Detector (TCD) to monitor molecular hydrogen. Hydrogen was analyzed with a Haysep Q packed column (2 m long, 1/8″ O.D.) at 45 °C connected to the TCD by using N_2 as a carrier gas. Once the complete reactor system was under pure N_2, the reaction was started by adding 3 vol. % of steam into the N_2 flow, which was sent in a continuous mode to the reactor. Pulses (of 0.5 mL each) from the reactor outlet were sent to the GC via a six-way valve during the reaction. The reaction continued until no hydrogen (from the water) was detected due to the complete oxidation of the oxide material. The reaction typically took 30 min.

All experimental work was conducted at the SABIC research centers of KAUST and Riyadh.

4. Conclusions

In this work, the extent of reduction by Ar ion sputtering of metal cations in CeO_2, $Ce_{0.95}Fe_{0.05}O_{2-\delta}$ and $Ce_{0.75}Fe_{0.25}O_{2-\delta}$ is studied by core and valence level spectroscopy. This is conducted to further study the reasons for the increased reaction rates of thermal water splitting when a fraction of Ce cations in CeO_2 are substituted with Fe cations. Ar ion sputtering resulted in an increase in the intensity of the Ce4f lines at about 1.5 eV below the Fermi level when compared to the O2p lines. Moreover, the XPS Ce5p/O2s ratio was found to be sensitive to the degree of reduction, which is attributed to a higher charge transfer from the oxygen to Ce ions upon reduction. This increase is concomitant with the increase in the XPS Ce3d spectra of the fraction of Ce^{3+}. Both increases are found to be higher for reduced $Ce_{0.95}Fe_{0.05}O_{2-\delta}$ when compared to $Ce_{0.75}Fe_{0.25}O_{2-\delta}$. On the other hand, the XPS Fe2p spectra showed no preferential increase between the two mixed oxides. Because water splitting to molecular hydrogen was found to be higher on $Ce_{0.95}Fe_{0.05}O_{2-\delta}$ than on $Ce_{0.75}Fe_{0.25}O_{2-\delta}$, it is postulated that the active sites for the reaction are those of Ce^{3+} cations and not metallic Fe.

References

1. Trovarelli, A. Catalytic Properties of Ceria and CeO$_2$-Containing Materials. *Catal. Rev. Sci. Eng.* **1996**, *38*, 439–520. [CrossRef]
2. Yang, C.; Lu, Y.; Zhang, L.; Kong, Z.; Yang, T.; Tao, L.; Zou, Y.; Wang, S. Defect Engineering on CeO$_2$-Based Catalysts for Heterogeneous Catalytic Applications. *Small Struct.* **2021**, *2*, 2100058. [CrossRef]
3. Torrente-Murciano, L.; Garcia-Garcia, R.R. Effect of nanostructured support on the WGSR activity of Pt/CeO$_2$ catalysts. *Catal. Commun.* **2015**, *71*, 1–6. [CrossRef]
4. Idriss, H. Oxygen vacancies role in thermally driven and photon driven catalytic reactions. *Chem. Catal.* **2022**, *2*, 1549–1560. [CrossRef]
5. Onigbajumo, A.; Swarnkar, P.; Will, G.; Sundararajan, T.; Taghipour, A.; Couperthwaite, S.; Steinberg, T.; Rainey, T. Techno-economic evaluation of solar-driven ceria thermochemical water-splitting for hydrogen production in a fluidized bed reactor. *J. Clean. Prod.* **2022**, *371*, 133303. [CrossRef]
6. Chueh, W.C.; Falter, C.; Abbott, M.; Scipio, D.; Furler, P.; Haile, S.M.; Steinfeld, A. High-flux solar-driven thermochemical dissociation of CO$_2$ and H$_2$O using nonstoichiometric ceria. *Science* **2010**, *330*, 797–801. [CrossRef]
7. Alifanti, M.; Baps, B.; Blangenois, N.; Naud, J.; Grange, P.; Delmon, B. Characterization of CeO$_2$-ZrO$_2$ Mixed Oxides. Comparison of the Citrate and Sol-Gel Preparation Methods. *Chem. Mater.* **2003**, *15*, 395–403. [CrossRef]
8. Andersson, D.A.; Simak, S.I.; Skorodumova, N.V.; Abrikosov, I.A.; Johansson, B. Redox properties of CeO$_2$–MO$_2$ (M = Ti, Zr, Hf, or Th) solid solutions from first principles calculations. *Appl. Phys. Lett.* **2007**, *90*, 031909. [CrossRef]
9. Diagne, C.; Idriss, H.; Kiennemann, A. Hydrogen Production by Ethanol Reforming over Rh/CeO$_2$-ZrO$_2$ Catalysts. *Catal. Commun.* **2002**, *3*, 565–571. [CrossRef]
10. Grau-Crespo, R.; de Leeuw, N.H.; Hamad, S.; Waghmare, U.V. Phase separation and surface segregation in ceria–zirconia solid solutions. *Proc. R. Soc. A* **2011**, *467*, 1925–1938. [CrossRef]
11. Hanken, B.E.; Stanek, C.R.; Grønbech-Jensen, N.; Asta, M. Computational study of the energetics of charge and cation mixing in U$_{1-x}$Ce$_x$O$_2$. *Phys. Rev. B* **2011**, *84*, 085131. [CrossRef]
12. Scaranto, G.; Idriss, H. The Effect of Uranium Cations on the Redox Properties of CeO2 Within the Context of Hydrogen Production from Water. *Top. Catal.* **2015**, *58*, 143–148. [CrossRef]
13. Al-Shankiti, I.; Al-Otaibi, F.; Al-Salik, Y.; Idriss, H. Solar thermal hydrogen production from water over modified CeO$_2$ materials. *Top. Catal.* **2013**, *56*, 1129–1138. [CrossRef]
14. Prieur, D.; Vigier, J.-F.; Popa, K.; Walter, O.; Dieste, O.; Varga, Z.; Beck, A.; Vitova, T.; Scheinost, A.; Martin, P. Charge distribution in U$_{1-x}$Ce$_x$O$_{2+y}$ nanoparticles. *Inorg. Chem.* **2021**, *60*, 14550–14556. [CrossRef] [PubMed]
15. Gupta, A.; Waghmare, U.V.; Hegde, M.S. Correlation of Oxygen Storage Capacity and Structural Distortion in Transition-Metal-, Noble-Metal-, and Rare-Earth-Ion-Substituted CeO$_2$ from First Principles Calculation. *Chem. Mater.* **2010**, *22*, 5184–5198. [CrossRef]
16. Gupta, A.; Kumar, A.; Waghmare, U.V.; Hegde, M.S. Origin of activation of Lattice Oxygen and Synergistic Interaction in Bimetal-Ionic Ce$_{0.89}$Fe$_{0.1}$Pd$_{0.01}$O$_{2-\delta}$ Catalyst. *Chem. Mater.* **2009**, *21*, 4880–4891. [CrossRef]
17. Al-Taweel, S.; Nadeem, M.A.; Idriss, H. A study of Ce$_x$Fe$_{1-x}$O$_2$ as a reducible oxide for the thermal hydrogen production from water. *Energy Technol.* **2022**, *10*, 2100491. [CrossRef]
18. Cheng, L.; Yue, X.; Fan, J.; Xiang, Q. Site-Specific Electron-Driving Observations of CO$_2$-to-CH$_4$ Photoreduction on Co-Doped CeO$_2$/Crystalline Carbon Nitride S-Scheme Heterojunctions. *Adv. Mater.* **2022**, *34*, 2200929. [CrossRef]
19. Zhao, S.; Kang, D.; Liu, Y.; Wen, Y.; Xie, X.; Yi, H.; Tang, X. Spontaneous Formation of Asymmetric Oxygen Vacancies in Transition-Metal-Doped CeO$_2$ Nanorods with Improved Activity for Carbonyl Sulfide Hydrolysis. *ACS Catal.* **2020**, *10*, 11739–11750. [CrossRef]
20. He, W.; Ran, J.; Yang, G.; He, Z.; Huang, X.; Crittenden, J. Promoting effect of Co-doped CeO$_2$ nanorods activity and SO$_2$ resistance for Hg^0 removal. *Fuel* **2022**, *317*, 123320. [CrossRef]
21. Ahn, K.; Yoo, D.S.; Prasad, D.H.; Lee, H.-W.; Chung, Y.-C.; Lee, J.-H. Role of Multivalent Pr in the Formation and Migration of Oxygen Vacancy in Pr-Doped Ceria: Experimental and First-Principles Investigations. *Chem. Mater.* **2012**, *24*, 4261–4267. [CrossRef]
22. Zhang, M.; Jiang, D.; Jiang, H. Enhanced oxygen storage capacity of Ce$_{0.88}$Mn$_{0.12}$O$_y$ compared to CeO$_2$: An experimental and theoretical investigation. *Mater. Res. Bull.* **2012**, *47*, 4006–4012. [CrossRef]
23. Krcha, M.D.; Janik, M.J. Examination of Oxygen Vacancy Formation in Mn-Doped CeO$_2$ (111) Using DFT+U and the Hybrid Functional HSE06. *Langmuir* **2013**, *29*, 10120–10131. [CrossRef] [PubMed]
24. Righi, G.; Benedetti, S.; Rita Magri, R. Investigation of the structural and electronic differences between silver and copper doped ceria using the density functional theory. *J. Phys. Condens. Matter.* **2022**, *34*, 204010. [CrossRef] [PubMed]
25. Nolan, M. Enhanced oxygen vacancy formation in ceria (111) and (110) surfaces doped with divalent cations. *J. Mater. Chem.* **2011**, *21*, 9160–9168. [CrossRef]
26. Wang, X.; Shen, M.; Wang, J.; Fabris, S. Enhanced Oxygen Buffering by Substitutional and Interstitial Ni Point Defects in Ceria: A First-Principles DFT+U Study. *J. Phys. Chem. C* **2010**, *114*, 10221–10228. [CrossRef]
27. Grieshammer, S.; Grope, B.O.H.; Koettgen, J.; Martin, M. A combined DFT + U and Monte Carlo study on rare earth doped ceria. *Phys. Chem. Chem. Phys.* **2014**, *16*, 9974–9986. [CrossRef]

28. Wang, H.; Qu, Z.; Xie, H.; Maeda, N.; Miao, L.; Wang, Z. Insight into the mesoporous $Fe_xCe_{1-x}O_{2-x}$ catalysts for selective catalytic reduction of NO with NH_3: Regulable structure and activity. *J. Catal.* **2016**, *338*, 56–67. [CrossRef]

29. Liu, X.-S.; Wang, X.-D.; Yao, M.; Cui, W.; Yan, H. Effects of Fe doping on oxygen vacancy formation and CO adsorption and oxidation at the ceria(111) surface. *Catal. Commun.* **2015**, *63*, 35–40. [CrossRef]

30. Lykaki, M.; Stefa, S.; Carabineiro, S.A.C.; Pandis, P.K.; Stathopoulos, V.N.; Konsolakis, M. Facet-Dependent Reactivity of Fe_2O_3/CeO_2 Nanocomposites: Effect of Ceria Morphology on CO Oxidation. *Catalysts* **2019**, *9*, 371. [CrossRef]

31. Kaneko, H.; Miura, T.; Ishihara, H.; Taku, S.; Yokoyama, T.; Nakajima, H.; Tamaura, Y. Reactive ceramics of $CeO_{2-x}MO_x$ (M = Mn, Fe, Ni, Cu) for H_2 generation by two-step water splitting using concentrated solar thermal energy. *Energy* **2007**, *32*, 656–663. [CrossRef]

32. Liang, C.; Ma, Z.; Lin, H.; Ding, L.; Qiu, J.; Frandsen, W.; Su, D. Template preparation of nanoscale $Ce_xFe_{1-x}O_2$ solid solutions and their catalytic properties for ethanol steam reforming. *J. Mater. Chem.* **2009**, *19*, 1417–1424. [CrossRef]

33. *Metal Oxide Nanostructures Chemistry: Synthesis from Aqueous Solutions*, 2nd ed.; Jolivet, J.-P. (Ed.) Chapter 5, Surface Chemistry and Physicochemistry of Oxides; Oxford University Press (2015) Editions EDP Sciences: Oxford, UK, 2015; pp. 181–226. [CrossRef]

34. Maslakov, K.I.; Teterin, Y.A.; Popel, A.J.; Teterin, A.Y.; Ivanov, K.E.; Kalmykov, S.N.; Petrov, V.G.; Petrov, P.K.; Farnan, I. XPS study of ion irradiated and unirradiated CeO_2 bulk and thin film Samples. *Appl. Surf. Sci.* **2018**, *448*, 154–162. [CrossRef]

35. Maslakov, K.I.; Teterin, Y.A.; Ryzhkov, M.V.; Ivanov, K.E.; Popel, A.J.; Teterin, A.Y.; Kalmykov, S.N.; Petrov, V.G.; Petrov, P.K.; Farnan, I. The electronic structure and the nature of the chemical bond in CeO_2. *Phys. Chem. Chem. Phys.* **2018**, *20*, 16167–16175. [CrossRef]

36. Eck, S.; Castellarin-Cudia, C.; Surnev, S.; Ramsey, M.G.; Netzer, F.P. Growth and thermal properties of ultrathin cerium oxide layers on Rh(111). *Surf. Sci.* **2002**, *520*, 173–185. [CrossRef]

37. Soria, E.; Román, E.; Williams, E.M.; de Segovia, J.L. Observations with synchrotron radiation (20–120 eV) of the TiO_2(110)–glycine interface. *Surf. Sci.* **1999**, *433–435*, 543–548. [CrossRef]

38. Parkinson, G.S. Iron oxide surfaces. *Surf. Sci. Rep.* **2016**, *71*, 272–365. [CrossRef]

39. Mansour, A.N.; Brizzolara, R.A. Characterization of the Surface of FeO Powder by XPS. *Surf. Sci. Spectra* **1996**, *4*, 345–350. [CrossRef]

40. Preisinger, M.; Krispin, M.; Rudolf, T.; Horn, S.; Strongin, D.R. Electronic structure of nanoscale iron oxide particles measured by scanning tunneling and photoelectron spectroscopies. *Phys. Rev. B* **2005**, *71*, 165409. [CrossRef]

41. Radu, T.; Iacovita, C.; Benea, D.; Turcu, R. X-Ray Photoelectron Spectroscopic Characterization of Iron Oxide Nanoparticles. *Appl. Surf. Sci.* **2017**, *405*, 337–343. [CrossRef]

42. Grosvenor, A.P.; Kobe, B.A.; McIntyre, N.S. Studies of the oxidation of iron by water vapour using X-ray photoelectron spectroscopy and QUASES. *Surf. Sci.* **2004**, *572*, 217–227. [CrossRef]

43. Temesghen, W.; Sherwood, P.M.A. Analytical utility of valence band X-ray photoelectron spectroscopy of iron and its oxides, with spectral interpretation by cluster and band structure calculations. *Anal. Bioanal. Chem.* **2002**, *373*, 601–608. [CrossRef] [PubMed]

44. Bagus, P.S.; Nelin, C.J.; Brundle, C.R.; Vincent Crist, C.B.; Lahiri, N.; Rosso, K.M. Combined multiplet theory and experiment for the Fe 2p and 3p XPS of FeO and Fe_2O_3. *J. Chem. Phys.* **2021**, *154*, 094709. [CrossRef] [PubMed]

45. Fondell, M.; Gorgoi, M.; Boman, M.; Lindblad, A. Surface modification of iron oxides by ion bombardment—Comparing depth profiling by HAXPES and Ar ion sputtering. *J. Electron Spectrosc. Relat. Phenom.* **2018**, *224*, 23–26. [CrossRef]